NANO LETTERS

Letter

pubs.acs.org/NanoLett

High-Operation-Temperature Plasmonic Nanolasers on Single-Crystalline Aluminum

Yu-Hsun Chou,[†,‡] Yen-Mo Wu,[‡] Kuo-Bin Hong,[‡] Bo-Tsun Chou,[§] Jheng-Hong Shih,[⊥] Yi-Cheng Chung,[⊥] Peng-Yu Chen,[§] Tzy-Rong Lin,[⊥,¶] Chien-Chung Lin,[†] Sheng-Di Lin,[§] and Tien-Chang Lu*[,‡]

[†]Institute of Lighting and Energy Photonics, National Chiao Tung University, Tainan 71150, Taiwan

[‡]Department of Photonics and [§]Department of Electronics Engineering, National Chiao Tung University, Hsinchu 300, Taiwan

[⊥]Department of Mechanical and Mechatronic Engineering and [¶]Institute of Optoelectronic Sciences, National Taiwan Ocean University, Keelung 202, Taiwan

Supporting Information

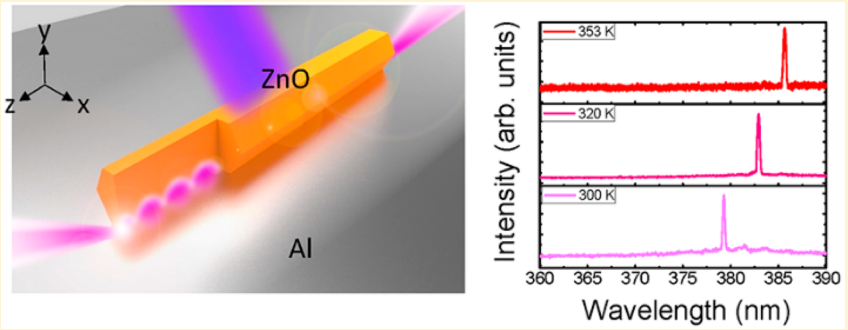

ABSTRACT: The recent development of plasmonics has overcome the optical diffraction limit and fostered the development of several important components including nanolasers, low-operation-power modulators, and high-speed detectors. In particular, the advent of surface-plasmon-polariton (SPP) nanolasers has enabled the development of coherent emitters approaching the nanoscale. SPP nanolasers widely adopted metal−insulator−semiconductor structures because the presence of an insulator can prevent large metal loss. However, the insulator is not necessary if permittivity combination of laser structures is properly designed. Here, we experimentally demonstrate a SPP nanolaser with a ZnO nanowire on the as-grown single-crystalline aluminum. The average lasing threshold of this simple structure is 20 MW/cm^2, which is four-times lower than that of structures with additional insulator layers. Furthermore, single-mode laser operation can be sustained at temperatures up to 353 K. Our study represents a major step toward the practical realization of SPP nanolasers.

KEYWORDS: *Nanolaser, surface plasmon, ZnO, nanowire, aluminum*

Surface plasmons (SPs) are electromagnetic surface waves traveling at the metal−dielectric interface. Since the concept of applying SPs to shrink the optical mode volume under the diffraction limit was introduced to the field of coherent light-emitting devices,[1,2] several novel types of nanoscale light emitters have been developed.[3−13] In application of SP (or surface-plasmon-polariton, SPP) lasers, the optical field can be strictly confined at the interface, which increases the probability for interaction between SPPs and gain material and results in a larger Purcell factor than that obtained in traditional photon laser devices.[14−17] Therefore, practical SPP nanolasers can provide researchers a valuable opportunity to expand the frontier of subwavelength applications such as quantum information, optical storage, subwavelength imaging, plasmonic circuits, and biosensing.[18−21] SPP nanolasers have been proposed and demonstrated in several designs.[6−14,17,21−24] A common method for realizing SPP lasers is the application of the hybrid plasmon mode to plasmonic devices by using a metal−insulator−semiconductor structure, which has been widely developed in the ultraviolet (UV) to visible regimes.[6−13,17,25] For a gain material with a bandgap energy less than 2.3 eV, gold is a common choice for plasmonic devices.[19−23] By contrast, silver (Ag) and aluminum (Al) are suitable for green to UV applications with larger bandgap materials, which possess several favorable exciton emission characteristics and can thus act as a suitable test bed for exploring quantum plasmonic effects[26] such as ultrafast modulation[13] and strong interaction between the exciton and SPP.[27,28]

The purpose of adding an insulator gap layer is to mitigate the large metal losses occurring in the metallically plasmonic waveguide so that the optical energy can be stored in an ultrasmall region with low propagation loss.[5,6,8−13,29] The

Received: February 6, 2016
Revised: April 7, 2016
Published: April 18, 2016

DOI: 10.1021/acs.nanolett.6b00537
Nano Lett. 2016, 16, 3179−3186

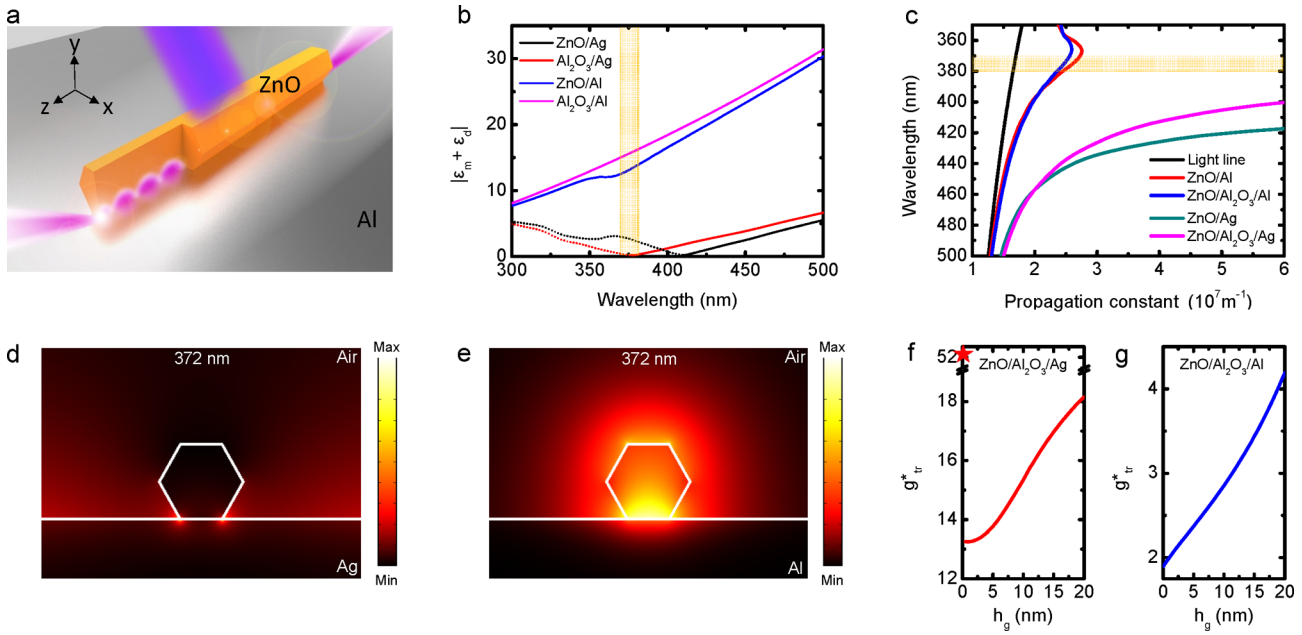

Figure 1. Structure, dispersion, mode profiles, and calculated transparency gain of ZnO SPP nanolasers. (a) Schematic of an SPP nanolaser containing a ZnO nanowire directly placed on the Al film. The pumping laser beam was incident from the top, and the coherent SPPs were amplified at the interface between the ZnO nanowire and the Al film. The radiated photons originated from the discontinuity at both facets of ZnO nanowires for optical detection. (b) Permittivity combination of oxide materials and metals as a function of light wavelength. When $|\varepsilon_m + \varepsilon_d|$ decreases, k_{sp} and k_y increase and so does the confinement factor. The dashed curves represent the conditions under which the SPP mode cannot be sustained. The shaded area represents the emission wavelength range of ZnO. (c) Dispersion curves of fundamental SPP modes for ZnO nanowires on different materials. The shaded area represents the emission wavelength range of ZnO. (d, e) Calculated electric field profiles $|E|$ of ZnO/Ag and ZnO/Al structures for 372 nm, respectively. The white hexagons in the figures indicate the cross-section of ZnO nanowires. The side length of the hexagonal ZnO nanowire was assumed to be 30 nm. (f, g) Calculated normalized transparency gains g_{tr}^* of the ZnO SPP nanolasers operated at 372 nm, with different insulator layer thicknesses. The normalized transparency gain is expressed as $g_{tr}^* = (L_p^* \Gamma_{wg})^{-1}$, where $L_p^* = L_p/\lambda$ is the normalized propagation length, and Γ_{wg} is the waveguide confinement factor. The lowest transparency gain was obtained when the insulator thickness was zero for the Al film, whereas the optimal insulator thickness was required for Al_2O_3 for the Ag film. For an insulator-free structure on the Ag film, the transparency gain increased dramatically, as denoted by the asterisk mark in the figure, because the SPP mode was leaky for that structure.

optical confinement factor, which describes the ratio of light overlapped with the gain material, is another key factor influencing the transparency gain. The confinement factor and propagation loss are determined by the characteristic wavenumbers of the SPP mode. Typically, the wavenumbers of an SPP wave in the propagation and transverse directions of a 2-D slab are inversely proportional to the square root of permittivity, that is, k_{sp}, $k_y \propto (\varepsilon_m + \varepsilon_d)^{-1/2}$, where ε_m and ε_d are the permittivities of the metal and dielectric material, respectively. Because the real part of ε_m is negative in ranges lower than the plasma frequency and ε_d is positive in the operation frequency range, carefully selecting materials with the most suitable combination of ε_m and ε_d for generating a low-loss SPP wave with a high optical confinement factor is essential. In this study, we showed that a SPP nanolaser can be constructed without inserting an artificial insulator layer between the active gain material and the metal film and that a low transparency gain can be maintained if the permittivity combination is designed properly.

Results and Discussion. Figure 1, panel a shows a nanolaser developed using a hexagonal ZnO nanowire placed on a metal film. Because the reported emission wavelength of ZnO lies in the range 370−380 nm,[30] Ag and Al are suitable metals for SPP generation.[31−33] The absolute values of the sum of these common oxide/metal structures constructed using a metal film (Ag or Al) and an oxide material (Al_2O_3 or ZnO), $|\varepsilon_m + \varepsilon_d|$, for light wavelengths from the UV to visible regimes are illustrated in Figure 1, panel b.[34−37] The absolute values of the permittivities for ZnO/Ag and Al_2O_3/Ag structures have minima near the wavelengths of 410 and 376 nm, respectively. These minimal wavelengths determine the SP wavelength (frequency), hence, only if the targeted operation wavelength for the SPP mode located at the right-hand sides of these minimal wavelengths holds the condition suitable for sustaining the SPP wave. Conversely, the absolute value of permittivity for Al combined with ZnO or Al_2O_3 shows no minima in the wavelength range, and for ZnO on Al, the SPP wave can always survive at the interface in the wavelength range between 300 and 500 nm. Here, we applied a simple and valid model to describe the criteria, but for accurate solutions, a complete 2-D/3-D model shall be required for either analytical or numerical solutions we shall demonstrate later.[38]

To facilitate considering the small dimension effect of the nanowire, Figure 1, panel c shows the calculated dispersion curves of fundamental SPP modes for the ZnO nanowire placed on different materials. The characteristics of ZnO nanolasers were calculated using the commercial finite-element-method software (COMSOL Multiphysics). The figure shows that the dispersion curve for ZnO/Ag (or ZnO/Al_2O_3/Ag) bends severely against the light line as the wavelength approaches the SPP wavelength. Therefore, the corresponding calculated electric field profile of 372 nm for the ZnO nanowire placed directly on Ag, as shown in Figure 1, panel d, demonstrates a leaky mode profile, which results in a massive transparency gain, as shown in Figure 1, panel f. To overcome this problem, a suitable intermediate insulator must be inserted between ZnO

DOI: 10.1021/acs.nanolett.6b00537
Nano Lett. 2016, 16, 3179−3186

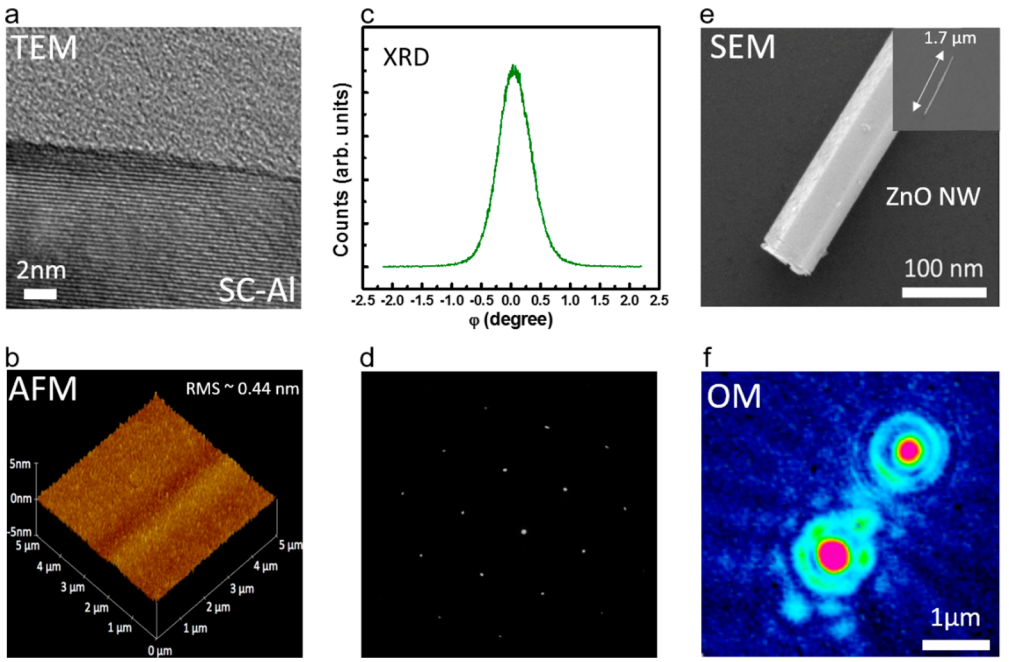

Figure 2. Crystalline and surface quality of the ZnO SPP laser. (a) TEM image of the high-quality single-crystalline Al film. The well-organized atoms shown on the bottom half, hardly seen native oxide on the surface, and the large grain boundaries ensure excellent optical properties of the MBE-grown Al film. (b) AFM image of an area of 5 × 5 μm^2 on the as-grown Al film. The RMS roughness of the surface was 0.44 nm. (c, d) X-ray diffraction curve with an fwhm of 0.7° and the selected-area electron diffraction pattern of the as-grown Al film, which confirmed that the film was single crystalline and had favorable structural characteristics. (e) SEM image of a ZnO nanowire placed on the as-grown Al film with a nanowire length of 1.7 μm. (f) Corresponding microscope image obtained at a power higher than the threshold condition showing the coherent light scattered from the two ends of the nanowire with a clear interference image.

and Ag because the minimal point of permittivity for Al_2O_3/Ag located at approximately 376 nm can facilitate proper SPP generation since the oxide material has a lower refractive index.[6,13,17,25] Consequently, properly selecting the insulator and optimal thickness is necessary. By contrast, the electric field can be well confined at the ZnO−Al interface, as shown in Figure 1, panel e. By analyzing the propagation length and confinement factor, the minimal transparency gain occurs when ZnO is directly placed on the Al, as shown in Figure 1, panel g. Such a simple nanolaser structure can facilitate fabrication and realization of direct electric excitation with more efficient thermal dissipation. Moreover, Al is compatible with the current silicon process, indicating the considerable potential for integrating the device into silicon-based photonic or plasmonic circuits.[39]

To demonstrate such a simple nanolaser structure, a high-quality Al film with single-crystalline characteristics grown through molecular beam epitaxy (MBE) was used to reduce scattering losses caused by the rough surface morphology and metallic losses originating from the polycrystalline grain.[12,17,40,41] Figure 2, panel a shows a transmission electron microscope (TEM) cross-section image of the as-grown high-quality Al film. The dense packing of the Al atoms prevents the rest of the layer from quick oxidation (Supporting Information). The root−mean−square (RMS) roughness of the as-grown Al film surface was measured through atomic force microscopy (AFM) in a 5 × 5 μm^2 area, as shown in Figure 2, panel b. The as-grown single-crystalline Al provided superior surface flatness, and the RMS roughness was 0.44 nm. The X-ray diffraction measurement and selective area electron diffraction pattern shown in Figure 2, panels c and d, respectively, indicate that the as-grown Al film exhibits high single crystallinity. The typical length of a ZnO nanowire ranged from 1−4 μm, as shown in Figure 2, panel e, and the side length of the cross-section hexagon was approximately 30 nm. The position of a single ZnO nanowire was targeted using a scanning electron microscope (SEM).

Figure 3, panels a and b, respectively, show the 77 and 300 K emission spectra of a 1.7-μm-long ZnO nanowire on the as-grown Al film. The corresponding light−light (L−L) curves are shown in Figure 3, panels c and d. The output intensity dramatically increased at P_{th} = 16 MW/cm^2 and 105 MW/cm^2, and the single emission line width narrowed from 16 to 0.2 nm at the temperatures 77 and 300 K, respectively, clearly demonstrating the crossover of the threshold condition. The polarization angles shown in the insets of Figure 3, panels c and d aligned with the nanowire direction, indicating that the single lasing mode belonged to the fundamental SP mode.[5,6,17] Figure 3, panel e shows the temperature-dependent emission spectra of a single ZnO nanolaser with the operation temperature increasing from 77 to 353 K at lasing powers higher than the threshold. The realization of robust high-operation-temperature nanolasers can be attributed to the high crystal quality of the as-grown Al film, large exciton oscillator strength of ZnO, and simple nanolaser structures, which provided a smaller transparency gain and more efficient thermal dissipation. The lasing peaks shown in Figure 3, panel e follow the ZnO exciton's Varshni trend in the heating process from 77 to 353 K, showing a redshift from 372 to 386 nm.[30] The emission peaks are in substantial contrast to the laser emission from electron−hole plasma (Supporting Information). The exciton emission characteristic originated from the rapid decay of carriers due to the strong interaction between the ZnO exciton and SPP, which could result in the estimated exciton density at powers

DOI: 10.1021/acs.nanolett.6b00537
Nano Lett. 2016, 16, 3179−3186

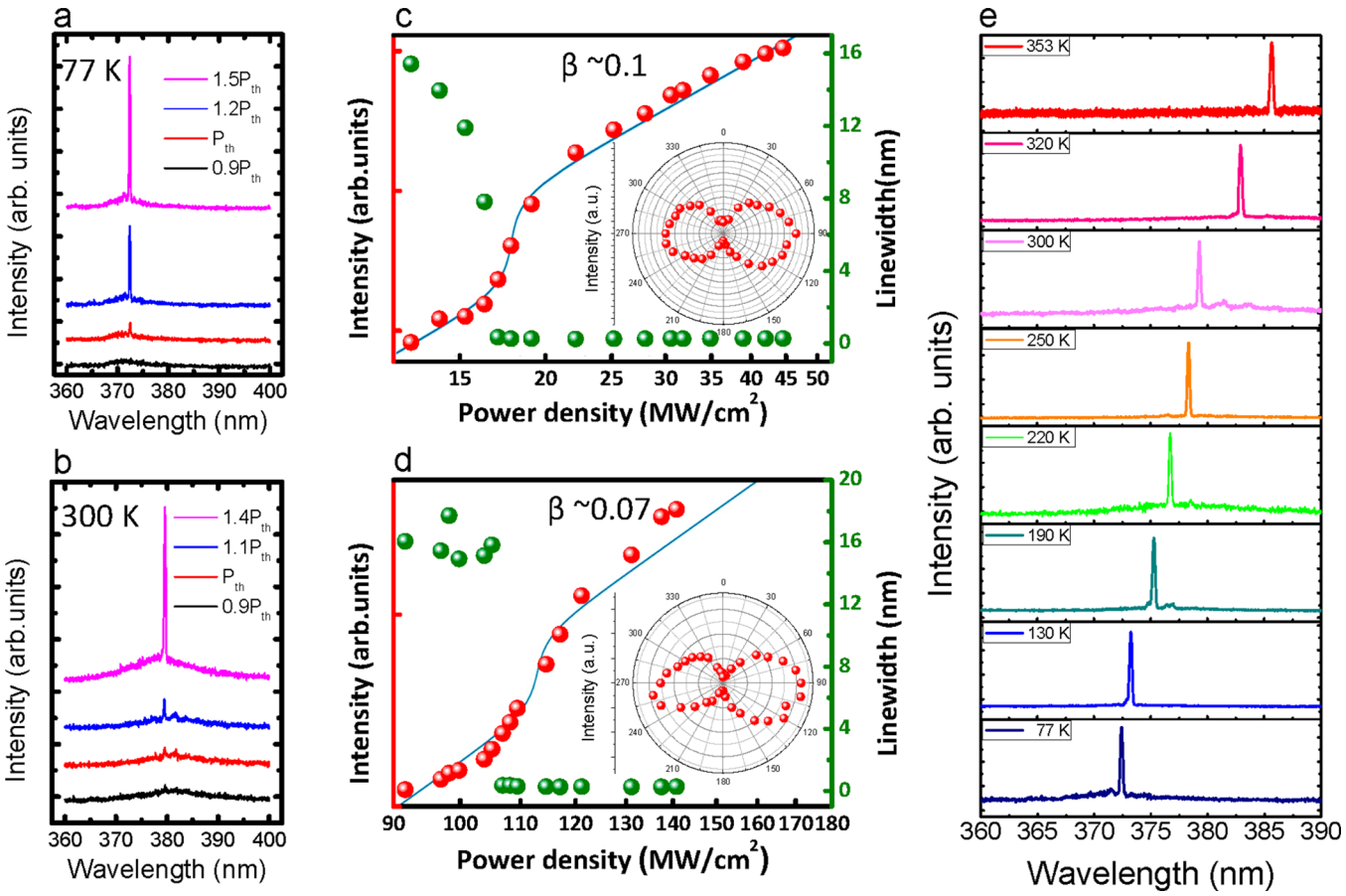

Figure 3. Lasing characteristics of the ZnO SPP nanolasers. (a, b) Spectra of a 1.7-μm-long ZnO nanowire placed directly on the as-grown Al film pumped at 77 and 300 K, respectively. The threshold values at 77 and 300 K were approximately 16 MW/cm^2 and 110 MW/cm^2. (c, d) Corresponding L−L curves (red spheres) and line width of dominant peaks (green spheres) of panels a and b. The solid lines are the fitted results calculated using the simplified rate equations. The extracted spontaneous coupling factors (β) are 0.1 and 0.07 at 77 and 300 K. The insets show the measured polarization distribution on top of the ZnO SPP nanolasers in the polar plots. The polarization direction was parallel to the nanowire direction with degrees of polarization of 93% and 81% at 77 and 300 K. The slightly asymmetric polar plots could be due to the fluctuated pulse laser source and long measurement time. (e) Evolution of the lasing spectra with the temperature increasing up to 353 K. The characteristic temperature was estimated to be 146 K (Supporting Information), clearly showing that the device has a wide operation temperature range.

higher than the lasing threshold being lower than the Mott density of ZnO (Supporting Information).[17,30,42−44]

We then compared the laser performance of the Al film with an additional deposited 5 nm-thick Al_2O_3 insulator layer. As shown in Figure 4, panel a, the average threshold power of the ZnO nanowires on as-grown Al was approximately 20 MW/cm^2, which is four-times lower than that of the samples with a deposited 5 nm-thick Al_2O_3 insulator layer. This is clearly explained by Figure 4, panel b, which shows the properties of the propagation length and confinement factor as a function of the insulator thickness. Although the propagation length decreases with decreasing the insulator layer thickness, the relative confinement factor is sufficiently large to confine the energy effectively, which results in the trend of decreasing transparency threshold gain with decreasing insulator layer thickness. In addition, without the additional deposited insulator layer, the sample surface can remain flat to reduce the loss caused by surface scattering, facilitating more uniform threshold performance of the device. Figure 4, panel c presents the electric fields of the fundamental SPP mode in the x−y plane. The symmetric charge distribution and intensive charge density along the y-direction in the ZnO/Al region enhanced the electric field inside the nanowire, which resulted in the electric field being polarized in the y-direction, and thus satisfies the characteristic of SPP resonance. The polarization of the fundamental SPP mode in the x−z plane is shown in Figure 4, panel d. The electric field of the fundamental mode is mainly polarized in the z-direction toward the nanowire axis, which results in a lasing action that scatters z-polarized radiation in the far field, as shown in Figure 4, panel e. The normalized mode volume, V_m, was estimated to be approximately 3.36 × 10^{-2} λ^3, which is smaller than that estimated for the 5 nm-thick insulator sample (3.68 × 10^{-2} λ^3). These values show that, although both structures can effectively shrink the electric field on a subwavelength scale, the nanolaser structure without an additional insulator layer can provide superior mode confinement because the fundamental SPP mode is directly generated at the interface between the ZnO nanowire and the Al film.

The Purcell factor, which is inversely proportion to the mode volume, is commonly used to evaluate the strength of interaction between light and matter; therefore, we investigated the exciton dynamics in the samples without and with the deposited insulators. We first measured the exciton decay time of ZnO nanowires on sapphire at different temperature to extract the radiative and nonradiative lifetime. As shown in Figure 5, panel a, a subnano-exciton decay time of $\tau \approx 260$ ps

DOI: 10.1021/acs.nanolett.6b00537
Nano Lett. 2016, 16, 3179−3186

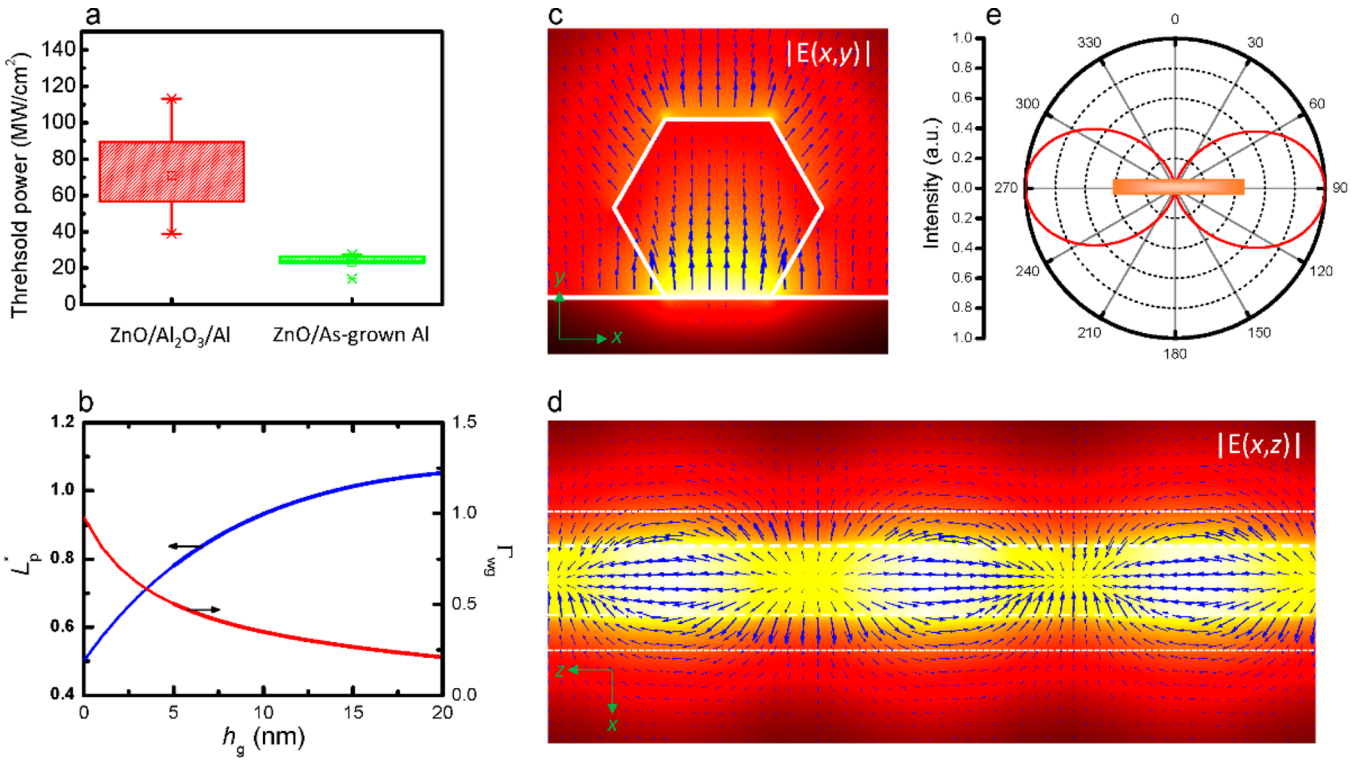

Figure 4. Threshold comparison and characteristics of fundamental SPP mode. (a) Quarter box chart of threshold density showing that the average threshold values of ten nanowires are 20 MW/cm^2 and 70 MW/cm^2 for the ZnO/as-grown Al and ZnO/Al_2O_3/Al nanolasers, respectively. The divergent threshold values existing in ZnO/Al_2O_3/Al nanolasers can be attributed to the fluctuating surface quality after the deposition of the insulator layer. (b) Calculated normalized propagation length and confinement factor of the fundamental SPP mode in the ZnO nanowire directly placed on the Al film. The rapidly increasing confinement factor can compensate for the propagation loss as the insulator thickness decreases, which results in the lowest threshold occurring at an insulator thickness of 0. (c) Electric field of the fundamental SPP mode in the ZnO nanowire directly placed on the Al film in the $x-y$ plane. (d) Resonant standing-wave pattern of the fundamental SPP mode oscillating along the ZnO nanowire in the $x-z$ plane. The arrows indicate the direction of the electric field. (e) Calculated far-field intensity radiating from the fundamental SPP mode in the ZnO nanowire directly placed on the Al film. The signals were collected on top of the ZnO nanowire. The central rod indicates the direction of the ZnO nanowire, which is parallel to the polarization direction.

and 248 ps for the ZnO nanowire at 10 and 77 K was obtained and decreased to 175 ps when the temperature was increased to 300 K because of an increase of the nonradiative recombination rate.[30] When the ZnO nanowire was placed on the Al film, the exciton decay times of samples without and with the 5 nm-thick deposited insulator decreased to 15 and 27 ps at 77 K, respectively, as shown in Figure 5, panel b. The estimated Purcell factors were 16.5 and 9.1 for the samples without and with the insulator layer when taking into account the nonradiative recombination and quenching effect (Supporting Information). This clearly explains the enhanced energy-exchange rate between the exciton and SPP in the nanolaser structure without the deposited insulator. As the temperature was increased to 300 K, the exciton decay times of the samples without and with the deposited insulator layer increased to 40 and 58 ps, yielding smaller Purcell factors of 4.3 and 3, respectively. The reduction in the measured Purcell factors at room temperature was due to the increased damping constant of the metal, nonradiative recombination, and quenching effect, which in turn contributed to a higher lasing threshold at a higher temperature. The contribution to the Purcell effect from SPPs mainly originates from the localized electric field enhancement of the mode. The calculated local Purcell factors for the nanolasers without and with the deposited insulator layer are shown in Figure 5, panels c and d.[6,17] The maximum local Purcell factors were 37.0 and 15.0 for the nanolasers without and with the deposited insulator layer, showing the same trend as that of the experimental results. The lower experimental Purcell factors can be attributed to the measured carrier lifetime being the average lifetime obtained from the entire nanowire. Nevertheless, the experimental Purcell factors reflected the lasing threshold trend.

Conclusions. We demonstrated that the threshold condition of the SPP nanolaser strongly depends on the permittivity combination of the metal and gain material. In particular, the additional insulator layer is not necessary for ZnO/Al plasmon nanolasers. The experimental results clearly demonstrated that the simple processed ZnO/as-grown Al plasmon nanolasers showed single-mode operation, a high operation temperature of up to 353 K, and an enhanced Purcell factor of up to 16.5. This simple nanolaser structure can exhibit low threshold gain and uniform laser performance, which is essential for high-temperature operation and the potential to be directly injected by a current source. The robustness of the ZnO nanowire directly placed on the as-grown Al film may provide opportunities for future nanolaser design, especially in electrical pumping applications and integration with the silicon process.

Methods. *Fabrication of ZnO Nanolasers.* We used the minimum-migration method to grow the highly flat single-crystalline Al film by MBE after a 200 nm-thick GaAs buffer layer was grown on the epi-ready GaAs (100) substrate.[33] Then

DOI: 10.1021/acs.nanolett.6b00537
Nano Lett. 2016, 16, 3179−3186

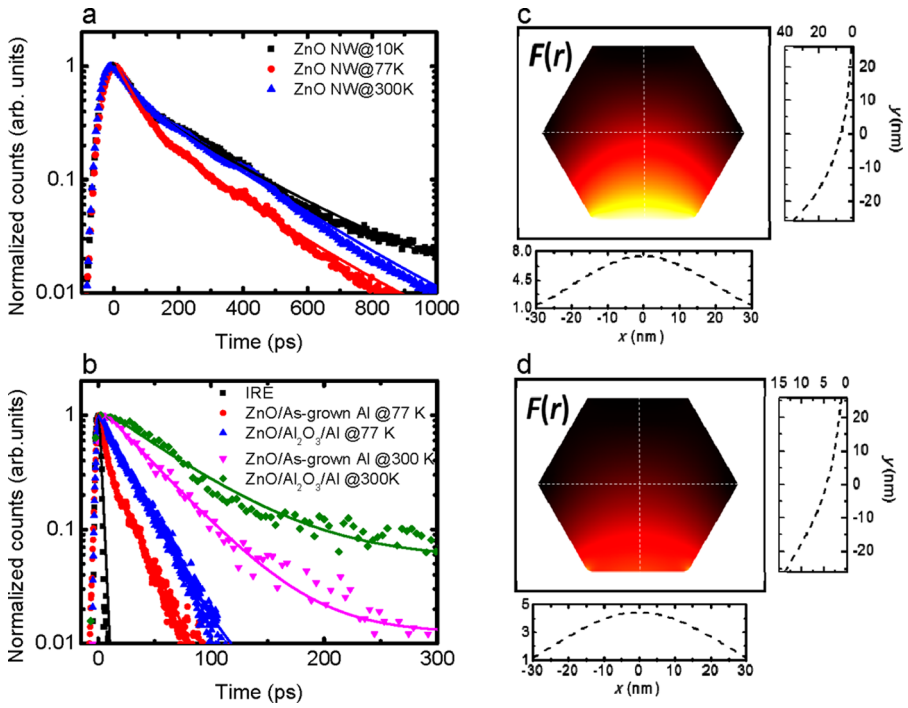

Figure 5. Exciton dynamics measured by time-resolved photoluminescence and calculated Purcell factors. (a) The exciton decay times of the typical ZnO nanowire placed on sapphire at 10 K, 77 K, and 300 K, fitted by double exponential decay, were approximately 260 ps, 248 ps, and 175 ps. (b) At 77 K, the exciton decay times of ZnO/as-grown Al and ZnO/Al_2O_3/Al were approximately 15 and 27 ps. The exciton decay times increased with the temperature and showed a longer lifetime of 40 ps for ZnO/as-grown Al and 58 ps for ZnO/Al_2O_3/Al. The system response time was approximately 6 ps. (c, d) Local Purcell factor distribution $F(r)$ inside the ZnO nanowire without and with 5 nm Al_2O_3 layers. The diagrams adjacent to and under the chart denote the local Purcell factor along the dashed lines in the *y*- and *x*-directions, respectively.

we kept the wafer at the growth temperature without the arsenic flux for 3 min. The original arsenic-rich template was converted to the gallium-rich template before the chamber was cooled to room temperature. The residual arsenic pressure was reduced to less than 1×10^{-10} Torr, and a 100 nm-thick Al layer was grown at approximately 0 °C with a growth rate of 0.05 nm/s to finish the single-crystalline Al template. For comparison, another template deposited with a 5 nm-thick Al_2O_3 dielectric layer by atomic layer deposition (ALD) on the Al film was made with the surface RMS rouness of 1.11 nm. To easily find out the position of the ZnO nanowires, we used the deep-UV lithography system and electron-gun (E-gun) evaporator to define several numbering gold patterns on templates. The high-quality single-crystalline ZnO nanowires were synthesized by hydrothermal method and were soaked in an isopropyl alcohol solution. We then sprayed the solution on the prepatterned templates with and without a deposited 5 nm-thick Al_2O_3 dielectric layer. The templates were kept in the nitrogen environment to prevent oxidation.

Measurement System. The nanolaser samples were mounted into a high vacuum chamber with a controlled temperature. The position of a single ZnO nanowire was targeted using a SEM before we accurately pumped the single ZnO nanowire by recognizing the gold pattern from the optical image of the measurement system. A charge coupled device (CCD) camera was installed for identifying the precise location of the nanowires. We then pumped the nanowire with a Nd:YVO_4 355 nm pulse laser with a 1-kHz repetition rate and a 0.5 ns pulse duration. A long working distance of a 100× near-UV infinity-corrected objective lens with a 0.55 numerical aperture was used for focusing the incident beam. A spot size of approximately 15 μm ensured that only the target nanowire was illuminated. Emissions from the nanowires were collected by the same path into a 600-μm core UV optical fiber and analyzed using a 320 mm single monochromator attached to a nitrogen-cooled CCD. The line width of our measurement results was restricted by the instrument's resolution of approximately 0.2 nm. The exciton decay time was measured by a streak camera pumped by a 76 MHz Ti:sapphire laser with the frequency tripled to 266 nm.

Simulation. The optical characteristics of ZnO nanolasers with and without an insulator layer observed in our experiments were calculated using commercial finite-element-method software (COMSOL Multiphysics). The refractive indices of Ag, ZnO, and the desired oxide materials were obtained from previous reports.[29−31,34] Perfectly matched layer conditions were considered. For more details about numerical simulations, please see the Supporting Information.

Rate Equation. To describe the dynamic evolution of the SPP nanolaser, we used a pair of coupled rate equations to calculate the change rate of exciton density n and SPP density s, which can be expressed as[17]

$$\frac{dn}{dt} = \eta\eta' P - An - \frac{n}{\tau_{nr}} - \frac{n}{\tau_{quench}} - g_0(n - n_{tr})s$$

$$\frac{ds}{dt} = \Gamma\beta An + \Gamma g_0(n - n_{tr})s - \gamma s$$

For simplifying the analysis, we considered only one SPP mode in the nanocavity and assumed the exciton distribution to be uniform in the nanowire. The terms η and η' denote the injection ratio and pump in ratio, respectively; P is the pumping density; A is the average spontaneous emission rate of the ZnO exciton; τ_{nr} and τ_{quench} are the nonradiative and quenching

DOI: 10.1021/acs.nanolett.6b00537
Nano Lett. 2016, 16, 3179−3186

lifetime, respectively. F is the effective Purcell factor; g_0 is the differential gain of ZnO and is proportional to the Purcell factor and group velocity of the SPP mode, where c is the speed of light in vacuum; γ refers to the SPP loss rate; and Γ is the waveguide confinement factor of the nanocavity.

■ ASSOCIATED CONTENT

Supporting Information

The Supporting Information is available free of charge on the ACS Publications website at DOI: 10.1021/acs.nanolett.6b00537.

Details of material analyze of nanolasers, temperature dependent on lasing characteristics, and surface plasmon mode simulation (PDF)

■ AUTHOR INFORMATION

Corresponding Author

*E-mail: timtclu@mail.nctu.edu.tw.

Notes

The authors declare no competing financial interest.

■ ACKNOWLEDGMENTS

The authors acknowledge the help of Prof. Shin-Chung Wang, Prof. Hao-Chung Kuo, Tsu-Chi Chang, and Pi-Ju Cheng at National Chiao Tung University. This work was partially supported by the Ministry of Education Aim for the Top University program and by Minister of Science and Technology (MOST) under Contract Nos. NSC100-2628-E009-013-MY3 and MOST 103-2221-E-019-028-MY3.

■ REFERENCES

(1) Bergman, D. J.; Stockman, M. I. Surface plasmon amplification by stimulated emission of radiation: Quantum generation of coherent surface plasmons in nanosystems. *Phys. Rev. Lett.* **2003**, *90* (2), 027402.

(2) Maier, S. A.; Kik, P. G.; Atwater, H. A.; Meltzer, S.; Harel, E.; Koel, B. E.; Requicha, A. A. G. Local detection of electromagnetic energy transport below the diffraction limit in metal nanoparticle plasmon waveguides. *Nat. Mater.* **2003**, *2* (4), 229−232.

(3) Ambati, M.; Nam, S. H.; Ulin-Avila, E.; Genov, D. A.; Bartal, G.; Zhang, X. Observation of Stimulated Emission of Surface Plasmon Polaritons. *Nano Lett.* **2008**, *8* (11), 3998−4001.

(4) Noginov, M. A.; Zhu, G.; Mayy, M.; Ritzo, B. A.; Noginova, N.; Podolskiy, V. A. Stimulated Emission of Surface Plasmon Polaritons. *Phys. Rev. Lett.* **2008**, *101* (22), 226806.

(5) Oulton, R. F.; Sorger, V. J.; Genov, D. A.; Pile, D. F. P.; Zhang, X. A hybrid plasmonic waveguide for sub-wavelength confinement and long-range propagation. *Nat. Photonics* **2008**, *2*, 496−500.

(6) Oulton, R. F.; Sorger, V. J.; Zentgraf, T.; Ma, R. M.; Gladden, C.; Dai, L.; Bartal, G.; Zhang, X. Plasmon lasers at deep subwavelength scale. *Nature* **2009**, *461* (7264), 629−632.

(7) Noginov, M. A.; Zhu, G.; Belgrave, A. M.; Bakker, R.; Shalaev, V. M.; Narimanov, E. E.; Stout, S.; Herz, E.; Suteewong, T.; Wiesner, U. Demonstration of a spaser-based nanolaser. *Nature* **2009**, *460* (7259), 1110−U68.

(8) Gramotnev, D. K.; Bozhevolnyi, S. I. Plasmonics beyond the diffraction limit. *Nat. Photonics* **2010**, *4*, 83−91.

(9) Ma, R. M.; Oulton, R. F.; Sorger, V. J.; Bartal, G.; Zhang, X. Room-Temperature Sub-Diffraction-Limited Plasmon Laser by Total Internal Reflection. *Nat. Mater.* **2011**, *10*, 110−113.

(10) Ding, K.; Ning, C. Z. Metallic Subwavelength-Cavity Semiconductor Nanolasers. *Light: Sci. Appl.* **2012**, *1*, e20.

(11) Khajavikhan, M.; Simic, A.; Katz, M.; Lee, J. H.; Slutsky, B.; Mizrahi, A.; Lomakin, V.; Fainman, Y. Thresholdless nanoscale coaxial lasers. *Nature* **2012**, *482* (7384), 204−207.

(12) Lu, Y. J.; Kim, J.; Chen, H. Y.; Wu, C. H.; Dabidian, N.; Sanders, C. E.; Wang, C. Y.; Lu, M. Y.; Li, B. H.; Qiu, X. G.; Chang, W. H.; Chen, L. J.; Shvets, G.; Shih, C. K.; Gwo, S. Plasmonic Nanolaser Using Epitaxially Grown Silver Film. *Science* **2012**, *337* (6093), 450−453.

(13) Sidiropoulos, T. P. H.; Roder, R.; Geburt, S.; Hess, O.; Maier, S. A.; Ronning, C.; Oulton, R. F. Ultrafast plasmonic nanowire lasers near the surface plasmon frequency. *Nat. Phys.* **2014**, *10* (11), 870−876.

(14) Andersen, M. L.; Stobbe, S.; Sorensen, A. S.; Lodahl, P. Strongly Modified Plasmon-Matter Interaction with Mesoscopic Quantum Emitters. *Nat. Phys.* **2011**, *7*, 215−218.

(15) Tame, M. S.; McEnery, K. R.; Ozdemir, S. K.; Lee, J.; Maier, S. A.; Kim, M. S. Quantum Plasmonics. *Nat. Phys.* **2013**, *9*, 329−340.

(16) de Leon, N. P.; Lukin, M. D.; Park, H. Quantum Plasmonic Circuits. *IEEE J. Sel. Top. Quantum Electron.* **2012**, *18*, 1781−1791.

(17) Chou, Y. H.; Chou, B. T.; Chiang, C. K.; Lai, Y. Y.; Yang, C. Y.; Li, H.; Lin, T. R.; Lin, C. C.; Kuo, H. C.; Wang, S. C.; Lu, T. C. Ultrastrong Mode Confinement in ZnO Surface Plasmon Nanolasers. *ACS Nano* **2015**, *9*, 3978−3982.

(18) Schuller, J. A.; Barnard, E. S.; Cai, W. S.; Jun, Y. C.; White, J. S.; Brongersma, M. L. Plasmonics for extreme light concentration and manipulation. *Nat. Mater.* **2010**, *9* (3), 193−204.

(19) Zijlstra, P.; Chon, J. W. M.; Gu, M. Five-Dimensional Optical Recording Mediated by Surface Plasmons in Gold Nanorods. *Nature* **2009**, *459*, 410−413.

(20) Anker, J. N.; Hall, W. P.; Lyandres, O.; Shah, N. C.; Zhao, J.; Van Duyne, R. P. Biosensing with plasmonic nanosensors. *Nat. Mater.* **2008**, *7* (6), 442−453.

(21) Hill, M. T.; Gather, M. C. Advances in small lasers. *Nat. Photonics* **2014**, *8*, 908−918.

(22) Suh, J. Y.; Kim, C. H.; Zhou, W.; Huntington, M. D.; Co, D. T.; Wasielewski, M. R.; Odom, T. W. Plasmonic Bowtie Nanolaser Arrays. *Nano Lett.* **2012**, *12* (11), 5769−5774.

(23) Zhou, W.; Dridi, M.; Suh, J. Y.; Kim, C. H.; Co, D. T.; Wasielewski, M. R.; Schatz, G. C.; Odom, T. W. Lasing action in strongly coupled plasmonic nanocavity arrays. *Nat. Nanotechnol.* **2013**, *8* (7), 506−511.

(24) van Beijnum, F.; van Veldhoven, P. J.; Geluk, E. J.; de Dood, M. J. A.; 't Hooft, G. W.; van Exter, M. P. Surface Plasmon Lasing Observed in Metal Hole Arrays. *Phys. Rev. Lett.* **2013**, *110* (20), 206802.

(25) Zhang, Q.; Li, G. Y.; Liu, X. F.; Qian, F.; Li, Y.; Sum, T. C.; Lieber, C. M.; Xiong, Q. H. A Room Temperature Low-Threshold Ultraviolet Plasmonic Nanolaser. *Nat. Commun.* **2014**, *5*, 4953.

(26) Gérard, D.; Gray, S. K. Aluminium Plasmonics. *J. Phys. D: Appl. Phys.* **2015**, *48*, 184001.

(27) Fofang, N. T.; Grady, N. K.; Fan, Z.; Govorov, A. O.; Halas, N. J. Plexciton Dynamics: Exciton-Plasmon Coupling in a J-Aggregate-Au Nanoshell Complex Provides a Mechanism for Nonlinearity. *Nano Lett.* **2011**, *11*, 1556−1560.

(28) Lawrie, B. J.; Kim, K. W.; Norton, D. P.; Haglund, R. F., Jr. Plasmon−Exciton Hybridization in ZnO Quantum-Well Al Nanodisc Heterostructures. *Nano Lett.* **2012**, *12*, 6152−6157.

(29) Dai, D.; He, S. A silicon-based hybrid plasmonic waveguide with a metal cap for a nano-scale light confinement. *Opt. Express* **2009**, *17*, 16646−16653.

(30) Ozgur, U.; Alivov, Y. I.; Liu, C.; Teke, A.; Reshchikov, M. A.; Dogan, S.; Avrutin, V.; Cho, S. J.; Morkoc, H. A comprehensive review of ZnO materials and devices. *J. Appl. Phys.* **2005**, *98* (4), 041301.

(31) West, P. R.; Ishii, S.; Naik, G. V.; Emani, N. K.; Shalaev, V. M.; Boltasseva, A. Searching for better plasmonic materials. *Laser Photonics Rev.* **2010**, *4* (6), 795−808.

(32) Knight, M. W.; King, N. S.; Liu, L.; Everitt, H. O.; Nordlander, P.; Halas, N. J. Aluminum for Plasmonics. *ACS Nano* **2014**, *8* (1), 834−840.

(33) Chou, B. T.; Chou, Y. H.; Wu, Y. M.; Chung, Y. C.; Hsueh, W. J.; Lin, S. W.; Lu, T. C.; Lin, T. R.; Lin, S. D. Single-crystalline aluminum film for ultraviolet plasmonic nanolasers. *Sci. Rep.* **2016**, *6*, 19887.

DOI: 10.1021/acs.nanolett.6b00537
Nano Lett. 2016, 16, 3179−3186

(34) Johnson, P. B.; Christy, R. W. Optical Constants of the Noble Metals. *Phys. Rev. B* **1972**, *6*, 4370−4379.
(35) Yoshikawa, H.; Adachi, S. Optical constants of ZnO. *Jpn. J. Appl. Phys.* **1997**, *36*, 6237−6243.
(36) Malitson, I. H.; Dodge, M. J. Refractive Index and Birefringence of Synthetic Sapphire. *J. Opt. Soc. Am.* **1972**, *62*, 1405.
(37) Gao, L.; Lemarchand, F.; Lequime, M. Exploitation of multiple incidences spectrometric measurements for thin film reverse engineering. *Opt. Express* **2012**, *20*, 15734−15751.
(38) Wan, L.; Huang, Y. M.; Dong, C. K.; Luo, H. J. Analytical solutions to zeroth-order dispersion relations of a cylindrical metallic nanowire near the backbending point. *Eur. Phys. J. B* **2012**, *85*, 17.
(39) Pavarelli, N.; Lee, J. S.; Rensing, M.; Scarcella, C.; Zhou, S.; Ossieur, P.; O'Brien, P. A. Optical and Electronic Packaging Processes for Silicon Photonic Systems. *J. Lightwave Technol.* **2015**, *33*, 991−997.
(40) Huang, J.-S.; Callegari, V.; Geisler, P.; Brüning, C.; Kern, J.; Prangsma, J. C.; Wu, X.; Feichtner, T.; Ziegler, J.; Weinmann, P.; Kamp, M.; Forchel, A.; Biagioni, P.; Sennhauser, U.; Hecht, B. Atomically flat single-crystalline gold nanostructures for plasmonic nanocircuitry. *Nat. Commun.* **2010**, *1*, 150.
(41) Liu, H. W.; Lin, F. C.; Lin, S. W.; Wu, J. Y.; Chou, B. T.; Lai, K. J.; Lin, S. D.; Huang, J. S. Single-Crystalline Aluminum Nanostructures on a Semiconducting GaAs Substrate for Ultraviolet to Near-Infrared Plasmonics. *ACS Nano* **2015**, *9*, 3875−3886.
(42) Johnson, J. C.; Yan, H. Q.; Yang, P. D.; Saykally, R. J. Optical cavity effects in ZnO nanowire lasers and waveguides. *J. Phys. Chem. B* **2003**, *107*, 8816−8828.
(43) Versteegh, M. A. M.; Vanmaekelbergh, D.; Dijkhuis, J. I. Room-Temperature Laser Emission of ZnO Nanowires Explained by Many-Body Theory. *Phys. Rev. Lett.* **2012**, *108*, 157402.
(44) Röder, R.; Wille, M.; Geburt, S.; Rensberg, J.; Zhang, M.; Lu, J. G.; Capasso, F.; Buschlinger, R.; Peschel, U.; Ronning, C. Continuous Wave Nanowire Lasing. *Nano Lett.* **2013**, *13* (8), 3602−3606.

DOI: 10.1021/acs.nanolett.6b00537
Nano Lett. 2016, 16, 3179−3186